Ionization of atomic hydrogen in strong infrared laser fields

Alexei N. Grum-Grzhimailo,[*] Brant Abeln,[†] Klaus Bartschat,[‡] and Daniel Weflen[§]
Department of Physics and Astronomy, Drake University, Des Moines, Iowa 50311, USA

Timothy Urness[‖]
Department of Mathematics and Computer Science, Drake University, Des Moines, Iowa 50311, USA
(Received 27 January 2010; published 14 April 2010)

We have used the matrix iteration method of Nurhuda and Faisal [Phys. Rev. A **60**, 3125 (1999)] to treat ionization of atomic hydrogen by a strong laser pulse. After testing our predictions against a variety of previous calculations, we present ejected-electron spectra as well as angular distributions for few-cycle infrared laser pulses with peak intensities of up to 10^{15} W/cm^2. It is shown that the convergence of the results with the number of partial waves is a serious issue, which can be managed in a satisfactory way by using the velocity form of the electric dipole operator in connection with an efficient time-propagation scheme.

DOI: 10.1103/PhysRevA.81.043408 PACS number(s): 32.80.Rm

I. INTRODUCTION

Atomic ionization in short-pulse high-intensity infrared laser fields has attracted significant interest from both experimentalists and theorists alike for about three decades, after pioneering articles on above-threshold ionization (ATI) and high-order harmonic generation (HHG) appeared in the late 1970s and 1980s. More recent studies include, for example, experiments by Rudenko *et al.* [1] and by Maharajan *et al.* [2] and theoretical investigations by Chen *et al.* [3] and by Madronero and Piraux [4].

In principle, a straightforward method to describe such processes is the numerical solution of the time-dependent Schrödinger equation (TDSE). Even with the dramatic increase in computational power over the past years, however, such an effectively exact solution continues to present significant challenges for long wavelengths, even in the dipole approximation for the laser-atom interaction and for the hydrogen atom with exactly known bound and continuum wave functions. A partial-wave close-coupling approach extensively used to treat this problem [5–11] faces serious difficulties because of the large ponderomotive energy and the number of partial waves that need to be coupled to get converged results. These difficulties can potentially also cause problems for the partial-wave expansion methods extended to photoionization of two-electron and even many-electron atoms [12–14] and molecules [15].

It is particularly difficult to obtain the angular distribution of the photoelectrons and other angle-differential observables that contain interference terms between different partial waves. Experience shows that it is nearly impossible for sufficiently high intensities to obtain convergence when employing the familiar, and easily usable, length form of the electric dipole operator. The latter is dominated by larger nuclear-electron distances in comparison with the velocity form. Therefore, employing the velocity form shows better promise with respect to obtaining converged results with a relatively small number of partial waves included in the close-coupling expansion of the total wave function. This fact was discussed and illustrated by Cormier and Lambropoulos [10]. However, the derivative operator appearing in this form presents new challenges in the time propagation of the wave function. These and other difficulties of solving the TDSE for a particle in a strong laser field were discussed in detail by Nurhuda and Faisal [16] and by Madronero and Piraux [4], and they are the principal motivation for the ongoing search for better algorithms for this problem.

The purpose of the present article, therefore, is to further analyze the capabilities of the promising matrix iterative method of Nurhuda and Faisal [16] that, to our knowledge, has not been used during the past decade for solving the TDSE. In Sec. II we describe the method (Sec. II A) and our implementation for the problem of interest, including the practical algorithm (Sec. II B). In addition, we introduce the observables of interest (Sec. II C), specifically the spectra and the angular distributions of photoelectrons produced in ionization of the hydrogen atom by long-wavelength laser pulses with different durations and intensities. Our results are presented and discussed in Sec. III, and we finish with a brief conclusion. Unless specified otherwise, atomic units are used throughout this article.

II. NUMERICAL METHOD

A. The matrix iterative approach

We use the matrix iterative method described in general terms by Nurhuda and Faisal [16] to solve the TDSE. To outline the approach in more detail, we begin by expanding the wave function of a particle characterized by the radius vector $\boldsymbol{r} = \{r, \vartheta, \varphi\}$ at time t as

$$\Psi(\boldsymbol{r}, t) = \sum_{\ell} b_\ell(r, t) Y_{\ell 0}(\Omega), \quad \Omega = \{\vartheta, \varphi\}. \tag{1}$$

[*]algrgr1492@yahoo.com; permanent address: Institute of Nuclear Physics, Moscow State University, Moscow 119991, Russia.
[†]brant.abeln@drake.edu
[‡]klaus.bartschat@drake.edu
[§]weflen@colorado.edu; now at Department of Physics, University of Colorado at Boulder, Boulder, Colorado 80309, USA.
[‖]timothy.urness@drake.edu

 ©2010 The American Physical Society

Assuming axial symmetry of the process with respect to the quantization z axis, only the spherical harmonics $Y_{\ell m}(\Omega)$ with $m = 0$ are left. Inserting Eq. (1) into the well-known Crank-Nicholson approximation of the short-time propagator

$$\Psi(\boldsymbol{r}, t + \Delta t) \approx \frac{1 - i\hat{H}\frac{\Delta t}{2}}{1 + i\hat{H}\frac{\Delta t}{2}}\Psi(\boldsymbol{r}, t) \tag{2}$$

yields

$$\sum_{\ell} b_{\ell}(r, t + \Delta t)Y_{\ell 0}(\Omega) = \frac{1 - i\hat{H}\frac{\Delta t}{2}}{1 + i\hat{H}\frac{\Delta t}{2}}\Psi(\boldsymbol{r}, t), \tag{3}$$

where $\hat{H}$ is the full Hamiltonian. Multiplying both sides of Eq. (3) by $Y^*_{\ell' 0}(\Omega)$, taking the integral over Ω, and using the orthogonality of the spherical harmonics gives

$$b_{\ell'}(r, t + \Delta t) = \int Y^*_{\ell' 0}(\Omega)\frac{1 - i\hat{H}\frac{\Delta t}{2}}{1 + i\hat{H}\frac{\Delta t}{2}}\Psi(\boldsymbol{r}, t)\, d\Omega. \tag{4}$$

In order to handle the right-hand side of Eq. (4), we introduce the Dirac δ function in the form

$$\delta(\Omega - \Omega') = \sum_{k} Y_{k0}(\Omega)Y^*_{k0}(\Omega') \tag{5}$$

and make the transformations

$$\begin{aligned}\left(1 - i\hat{H}\frac{\Delta t}{2}\right)\Psi(\boldsymbol{r}, t) &= \left(1 - i\hat{H}\frac{\Delta t}{2}\right)\sum_{\ell} b_{\ell}(r, t)Y_{\ell 0}(\Omega) \\ &= \int \sum_{k} Y_{k0}(\Omega)Y^*_{k0}(\Omega')\left(1 - i\hat{H}\frac{\Delta t}{2}\right) \\ &\quad \times \sum_{\ell} b_{\ell}(r, t)Y_{\ell 0}(\Omega')\, d\Omega' \\ &\equiv \sum_{k} \phi_k(r, t)Y_{k0}(\Omega),\end{aligned} \tag{6}$$

where

$$\phi_k(r, t) = b_k(r, t) - i\sum_{\ell} \langle Y_{k0}|\hat{H}|Y_{\ell 0}\rangle_r \frac{\Delta t}{2} b_{\ell}(r, t). \tag{7}$$

Here $\langle\,\rangle_r$ denotes the integration over the solid angle Ω, thereby leaving r as the argument. Thus we have from Eqs. (4) and (6)

$$b_{\ell'}(r, t + \Delta t) = \sum_{k} \langle Y_{\ell' 0}|\left(1 + i\hat{H}\frac{\Delta t}{2}\right)^{-1}|Y_{k0}\rangle_r \phi_k(r, t). \tag{8}$$

We now decompose the operator in Eq. (8) as

$$1 + i\hat{H}\frac{\Delta t}{2} = \hat{O}_{\mathrm{D}} + \hat{O}_{\mathrm{ND}}, \tag{9}$$

where $\hat{O}_{\mathrm{D}}$ is the diagonal part and $\hat{O}_{\mathrm{ND}}$ is the nondiagonal part with matrix elements

$$\hat{O}^{\ell}_{\mathrm{D}} = \langle Y_{\ell 0}|1 + i\hat{H}\frac{\Delta t}{2}|Y_{\ell 0}\rangle_r \tag{10}$$

and

$$\hat{O}^{\ell k}_{\mathrm{ND}} = \begin{cases} \langle Y_{\ell 0}|1 + i\hat{H}\frac{\Delta t}{2}|Y_{k0}\rangle_r & \ell \neq k, \\ 0 & \ell = k, \end{cases} \tag{11}$$

respectively. Expanding

$$\begin{aligned}(\hat{O}_{\mathrm{D}} + \hat{O}_{\mathrm{ND}})^{-1} &= \left(1 + \hat{O}^{-1}_{\mathrm{D}}\hat{O}_{\mathrm{ND}}\right)^{-1}\hat{O}^{-1}_{\mathrm{D}} \\ &= \left(1 - \hat{O}^{-1}_{\mathrm{D}}\hat{O}_{\mathrm{ND}} + \hat{O}^{-1}_{\mathrm{D}}\hat{O}_{\mathrm{ND}}\hat{O}^{-1}_{\mathrm{D}}\hat{O}_{\mathrm{ND}} - \cdots\right) \\ &\quad \times \hat{O}^{-1}_{\mathrm{D}}\end{aligned} \tag{12}$$

and substituting this expansion into Eq. (8) yields

$$b_{\ell'}(r, t + \Delta t) = \sum_{v} b^{(v)}_{\ell'}(r, t + \Delta t), \tag{13}$$

where

$$\begin{aligned}&b^{(v)}_{\ell'}(r, t + \Delta t) \\ &\quad = (-1)^v \sum_{k} \langle Y^*_{\ell' 0}|\left(\hat{O}^{-1}_{\mathrm{D}}\hat{O}_{\mathrm{ND}}\right)^v \hat{O}^{-1}_{\mathrm{D}}|Y_{k0}\rangle_r \phi_k(r, t).\end{aligned} \tag{14}$$

The first term ($v = 0$) is

$$b^{(0)}_{\ell'}(r, t + \Delta t) = \frac{1}{\hat{O}^{\ell'}_{\mathrm{D}}}\phi_{\ell'}(r, t), \tag{15}$$

since $\hat{O}_{\mathrm{D}}$ is diagonal. The second term can be evaluated after formally inserting two unitary operators but then use again the fact that $\hat{O}_{\mathrm{D}}$ is diagonal. The result is

$$\begin{aligned}b^{(1)}_{\ell'}(r, t + \Delta t) &= \sum_{k} \langle Y_{\ell' 0}| - \hat{O}^{-1}_{\mathrm{D}}\hat{O}_{\mathrm{ND}}\hat{O}^{-1}_{\mathrm{D}}|Y_{k0}\rangle_r \phi_k(r, t) \\ &= \frac{-1}{\hat{O}^{\ell'}_{\mathrm{D}}}\sum_{k} \langle Y_{\ell' 0}|\hat{O}_{\mathrm{ND}}|Y_{k0}\rangle_r \frac{1}{\hat{O}^{k}_{\mathrm{D}}}\phi_k(r, t) \\ &= \frac{-1}{\hat{O}^{\ell'}_{\mathrm{D}}}\sum_{k} \hat{O}^{\ell' k}_{\mathrm{ND}} b^{(0)}_{k}(r, t + \Delta t).\end{aligned} \tag{16}$$

Proceeding further along this line, we finally obtain the recursion relation (12) of Nurhuda and Faisal [16]

$$b^{(v)}_{\ell'}(r, t + \Delta t) = \frac{-1}{\hat{O}^{\ell'}_{\mathrm{D}}}\sum_{k} \hat{O}^{\ell' k}_{\mathrm{ND}} b^{(v-1)}_{k}(r, t + \Delta t), \tag{17}$$

with the convergence condition that

$$\gamma = \left|\frac{\hat{O}_{\mathrm{ND}}}{\hat{O}_{\mathrm{D}}}\right| < 1 \tag{18}$$

for all relevant matrix elements.

B. Application: Electron in an electromagnetic field

We are interested in describing an electron in an electromagnetic field with the full Hamiltonian given by

$$\hat{H} = -\frac{\nabla^2}{2} + V(r) - \frac{i}{c}\boldsymbol{A}(t)\cdot\boldsymbol{\nabla}, \tag{19}$$

where $V(r)$ is the static Coulomb potential while the vector potential $\boldsymbol{A}(t)$ is related to the external electric field $\boldsymbol{E}(t)$ through

$$\boldsymbol{A}(t) = -c\int_{-\infty}^{t} \boldsymbol{E}(t)\, dt, \tag{20}$$

with c denoting the speed of light in vacuum. Note that we omitted the term $\boldsymbol{A}^2(t)/2$ in (19), thus implying that the gauge transformation

$$\Psi(\boldsymbol{r}, t) \Rightarrow \exp\left[-\frac{i}{2}\int_{-\infty}^{t} \boldsymbol{A}^2(t')\, dt'\right]\Psi(\boldsymbol{r}, t) \tag{21}$$

has been performed [17]. We use the matrix iteration method for the velocity form of the electric dipole operator and imply a linearly polarized laser pulse, with the polarization direction of the electric field defining the z axis. Subsequently we also show some comparisons with results obtained in the length form $\boldsymbol{r}\cdot\boldsymbol{E}(t)$ of the interaction, for which we used the method described by Grum-Grzhimailo *et al.* [11].

We choose $\hat{O}_{\rm D}$ to contain the identity operator as well as all the terms of the field-free Hamiltonian [the first two terms in Eq. (19)] and $\hat{O}_{\rm ND}$ to contain the third interaction term in Eq. (19). This yields the matrix elements (10) and (11) as

$$\hat{O}_{\rm D}^{\ell}=1+i\left[-\frac{1}{2r^2}\frac{\partial}{\partial r}\left(r^2\frac{\partial}{\partial r}\right)+\frac{\ell(\ell+1)}{2r^2}+V(r)\right]\frac{\Delta t}{2} \tag{22}$$

and

$$\hat{O}_{\rm ND}^{\ell k}=\frac{A_z(t)}{c}\frac{\Delta t}{2}\langle Y_{\ell 0}|\frac{\partial}{\partial z}|Y_{k0}\rangle_r=\frac{A_z(t)}{c}\frac{\Delta t}{2}\left[\frac{\partial}{\partial r}C_{\ell k}+\frac{1}{r}\tilde{C}_{\ell k}\right], \tag{23}$$

where

$$C_{\ell k}=\frac{k}{\sqrt{(2k+1)(2k-1)}}\delta_{\ell,k-1}+\frac{k+1}{\sqrt{(2k+3)(2k+1)}}\delta_{\ell,k+1} \tag{24}$$

and

$$\tilde{C}_{\ell k}=\frac{k(k+1)}{\sqrt{(2k+1)(2k-1)}}\delta_{\ell,k-1}-\frac{k(k+1)}{\sqrt{(2k+3)(2k+1)}}\delta_{\ell,k+1}. \tag{25}$$

In order to carry out the algorithm, we introduce the functions

$$a_\ell(r,t)\equiv rb_\ell(r,t),\quad \bar{\phi}_\ell(r,t)\equiv r\phi_\ell(r,t) \tag{26}$$

and obtain from Eqs. (7), (22), and (23)

$$\hat{O}_{\rm ND}^{\ell k}b_k(r,t)=\frac{\Delta t}{2}\frac{A_z(t)}{c}\left[\frac{\partial}{\partial r}C_{\ell k}+\frac{1}{r}X_{\ell k}\right]a_k(r,t) \tag{27}$$

and

$$\bar{\phi}_\ell(r,t)=a_\ell(r,t)-i\frac{\Delta t}{2}\left[\frac{-1}{2}\frac{\partial^2}{\partial r^2}+\frac{\ell(\ell+1)}{2r^2}+V(r)\right]a_\ell(r,t)-\frac{A_z(t)}{c}\frac{\Delta t}{2}\sum_k\left[\frac{\partial}{\partial r}C_{\ell k}+\frac{1}{r}X_{\ell k}\right]a_k(r,t), \tag{28}$$

where $X_{\ell k}\equiv\tilde{C}_{\ell k}-C_{\ell k}$.

The algorithm for the time propagation is then as follows.

(i) Having at time t the wave function $\Psi(\boldsymbol{r},t)$ and, hence, the set of functions $a_\ell(r,t)$, find the functions $\bar{\phi}_\ell(r,t)$ from Eq. (28). Usually only functions with a single value of ℓ are nonzero at $t=0$. In our particular case, we start with the hydrogen atom in the $1s$ ground state.

(ii) After writing Eq. (15) in the form

$$\left[1+i\frac{\Delta t}{2}\left(\frac{-1}{2}\frac{\partial^2}{\partial r^2}+\frac{\ell(\ell+1)}{2r^2}+V(r)\right)\right]a_\ell^{(0)}(r,t+\Delta t)=\bar{\phi}_\ell(r,t), \tag{29}$$

calculate $a_\ell^{(0)}(r,t+\Delta t)$. To solve Eq. (29) we express the second derivative through a three-point finite-difference formula and then use the well-known backward substitution algorithm for tridiagonal matrices [18]. While this finite-difference method may not be as accurate as finite-element approaches used, for example, in Refs. [4,10], it seems accurate enough for our cases of interest and has an advantage when extending the calculation to high ejected-electron energies (see later in this article).

(iii) Using Eq. (27), find the function

$$\xi_\ell^{(1)}(r,t+\Delta t)=-r\sum_k\hat{O}_{\rm ND}^{\ell k}\frac{1}{r}a_k^{(0)}(r,t+\Delta t)=\frac{\Delta t}{2}\frac{A_z(t)}{c}\sum_k\left(\frac{\partial}{\partial r}C_{\ell k}+\frac{1}{r}X_{\ell k}\right)\times a_k^{(0)}(r,t+\Delta t), \tag{30}$$

which defines the right-hand side of Eq. (16).

(iv) From Eq. (16) written in a way identical to Eq. (29) with the substitutions $a_\ell^{(0)}(r,t+\Delta t)\to a_\ell^{(1)}(r,t+\Delta t)$ and $\bar{\phi}(r,t)\to\xi_\ell^{(1)}(r,t+\Delta t)$, find the functions $a_\ell^{(1)}(r,t+\Delta t)$.

(v) Repeat Eq. (30) with $a_k^{(0)}(r,t+\Delta t)\to a_k^{(1)}(r,t+\Delta t)$ to obtain $\xi_\ell^{(2)}(r,t+\Delta t)$ and use it in step (iv) to solve for $a_\ell^{(2)}(r,t+\Delta t)$. The iterations proceed until convergence of expansion (13) is reached. Once the set of $a_\ell(r,t+\Delta t)$ has been determined to acceptable accuracy, we can go back to (i) and continue to the next time step.

As pointed out by Nurhuda and Faisal [16], the number of iterations can be adjusted at every time step based on the behavior of the norm of the total wave function, and one can try to optimize the length of the time step and the number of iterations. In our applications, we always used five iterations and checked that our fixed time step was sufficiently small to keep the deviation of the norm from unity to less than 10^{-6}. Also, we used a large radial mesh to essentially keep the entire wave function in the box. The very small part that might escape and would then be reflected from the boundary was absorbed by a standard imaginary gobbler potential. Although some of these precautions may seem computationally expensive, they ensure numerical stability of the results. Runs for the cases shown in Sec. III typically took from a few hours to a few days on a single 2-GHz processor of a multinode cluster. We are in the process of parallelizing the code to reduce the wall time needed to get results, but the current situation is already acceptable.

C. Observables

We are interested in the ejected-electron spectrum, i.e., the angle-integrated probability density for finding a photoelectron with energy $\varepsilon=k^2/2$, as well as the angle-differential probability for such an electron being emitted into the direction specified by the solid-angle element $\Omega_{\boldsymbol{k}}=\{\Theta,\Phi\}$. In order to define these quantities, we expand the eigenfunction of the field-free Hamiltonian for the photoelectron propagating with linear momentum $\boldsymbol{k}$ in partial waves as

$$\Phi_{\boldsymbol{k}}^{-}(\boldsymbol{r})=\frac{4\pi}{r}\sum_{\ell m}i^\ell e^{-i\delta_{\varepsilon\ell}}P_{\varepsilon\ell}(r)Y_{\ell m}^*(\Theta,\Phi)Y_{\ell m}(\vartheta,\varphi), \tag{31}$$

For our case of the atomic hydrogen target, $P_{\varepsilon\ell}(r)$ is the energy-normalized regular Coulomb function while $\delta_{\varepsilon\ell} = \arg\ \Gamma(\ell + 1 - i/k)$ is the Coulomb phase.

The probability density for finding the photoelectron with energy ε emitted in the direction $\Omega_{\boldsymbol{k}} \equiv (\Theta, \Phi)$ is given by

$$\frac{d^2\mathscr{P}}{d\varepsilon d\Omega_{\boldsymbol{k}}} = \lim_{t\to\infty} |\langle \Phi_{\boldsymbol{k}}^{-}(\boldsymbol{r})|\Psi(\boldsymbol{r},t)\rangle|^2 = \frac{\mathscr{P}_\varepsilon}{4\pi}\left[1 + \sum_{L>0} \beta_L(\varepsilon) P_L(\cos\Theta)\right]. \quad (32)$$

Here $P_L(\cos\Theta)$ is a standard Legendre polynomial and $\mathscr{P}_\varepsilon$ is the angle-integrated probability density (i.e., the photoelectron energy spectrum),

$$\mathscr{P}_\varepsilon = \int d\Omega_{\boldsymbol{k}} \frac{d^2\mathscr{P}}{d\varepsilon d\Omega_{\boldsymbol{k}}}. \quad (33)$$

The anisotropy parameters, $\beta_L(\varepsilon)$ (subsequently we omit the argument ε), are given by

$$\beta_L = \frac{1}{\mathscr{P}_\varepsilon} \sum_{\ell\ell'} i^{\ell'-\ell} e^{i(\delta_{\varepsilon\ell} - \delta_{\varepsilon\ell'})} \nu_{\ell\ell'}^L Z_{\varepsilon\ell} Z_{\varepsilon\ell'}^*, \quad (34)$$

where $\nu_{\ell\ell'}^L = \nu_{\ell'\ell}^L = \sqrt{(2\ell+1)(2\ell'+1)}(\ell 0, \ell' 0|L0)$ with $(\ell 0, \ell' 0|L0)$ denoting a Clebsch-Gordan coefficient and

$$Z_{\varepsilon\ell} = \lim_{t\to\infty} \int_0^\infty P_{\varepsilon\ell}(r) a_\ell(r,t)\, dr, \quad (35)$$

so that

$$\mathscr{P}_\varepsilon = \sum_\ell |Z_{\varepsilon\ell}|^2. \quad (36)$$

The electron spectrum and the anisotropy parameters are calculated from the wave function at the end of the pulse and hence do not contain any information about the time when the electron was ejected. In order to get some information about this time dependence, we also show results for the electron density $\rho(\boldsymbol{r},t) \equiv \Psi^*(r,t)\Psi(\boldsymbol{r},t)$ at various times t during the pulse. This function shows when and where the electron might be moving, but it does not contain information about its energy. Hence, the two sets of functions contain complimentary information.

III. RESULTS AND DISCUSSION

Figure 1 shows the electric field $\boldsymbol{E}(t)$ and the vector potential $\boldsymbol{A}(t)$ of a simple test case, for which the ejected-electron spectrum was also presented by Madronero and Piraux [4]. Specifically, a four-cycle laser pulse with a $\sin^2$ envelope, a peak intensity of 1×10^{15} W/cm^2, and a central frequency of 0.3 a.u. (wavelength 152 nm) is used to ionize atomic hydrogen. This is essentially a two-photon process, and for this field strength and pulse length we see the main peak in Fig. 2 as well as one clearly visible above-threshold peak around an energy of 0.3 a.u., followed by another small maximum between 0.5 and 0.6 a.u.

This is not a particularly challenging numerical problem, and hence we get good agreement between the results obtained in the length and the velocity forms of the electric dipole operator. Also, although we included angular momenta of up to $\ell_{\max} = 20$ for both forms, we could get converged results

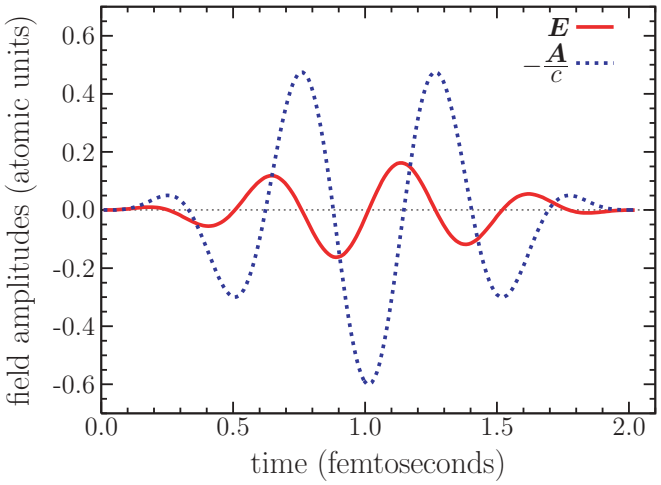

FIG. 1. (Color online) Electric field $\boldsymbol{E}(t)$ and vector potential $-\boldsymbol{A}(t)/c$ for a four-cycle laser pulse with a $\sin^2$ envelope for $\boldsymbol{E}(t)$, a peak intensity of 1×10^{15} W/cm^2, and a central frequency of 0.3 a.u., corresponding to a wavelength of 152 nm.

with significantly less in the velocity form (see later in this article).

Even for this rather simple problem, however, it is worth pointing out two interesting features. (i) The results exhibit a significant dependence on whether the simple $\sin^2$ envelope function is used for the vector potential $\boldsymbol{A}(t)$ or for the electric field $\boldsymbol{E}(t)$. (ii) When the vector potential is described by the $\sin^2$ envelope, the first peak is at the expected energy of just below 0.02 a.u. (in this case the ponderomotive energy is about 0.08 a.u.), but the subsequent peaks are *not* separated by a multiple of the photon energy. [Especially the second, though very small, ATI peak is clearly below 0.6 a.u.] Even more remarkable, however, is the fact that, if the $\sin^2$ envelope is used for the electric field, the first peak is clearly shifted to lower ejected-electron energies.

These results are due to the fact that the pulse is very short (only four cycles), and hence the derivative of the envelope function in $\boldsymbol{E}(t) = -\partial\boldsymbol{A}(t)/c\partial t$ is by no means negligible. Furthermore, the Keldysh parameter $\sqrt{I_p/2U_p}$, where I_p is the ionization energy and $U_p = I/4\omega^2$ is the ponderomotive energy for a laser intensity I and angular frequency ω, is less than 2 for this case, thus suggesting that this is no longer a simple multiphoton absorption process.

In addition to the spectrum, we also present our results for various angular distribution parameters for this case. We see significantly nonzero β parameters, with both even and odd indices. The nonvanishing values $\beta_1, \beta_3, \beta_5, \ldots$ indicate a significant dependence of the angular distribution on the carrier envelope phase, once again due to the strength and the short length of the pulse. We show sample angular distributions for fixed ejected-electron energies later in this article, as well as snapshots of the ejected-electron density as a function of time.

To check our code for more difficult situations, we then ran the cases presented in Fig. 10 of Chen *et al.* [3]. The electric field and the vector potential for one of the cases, a 20-cycle laser pulse with a $\sin^2$ envelope, a peak intensity

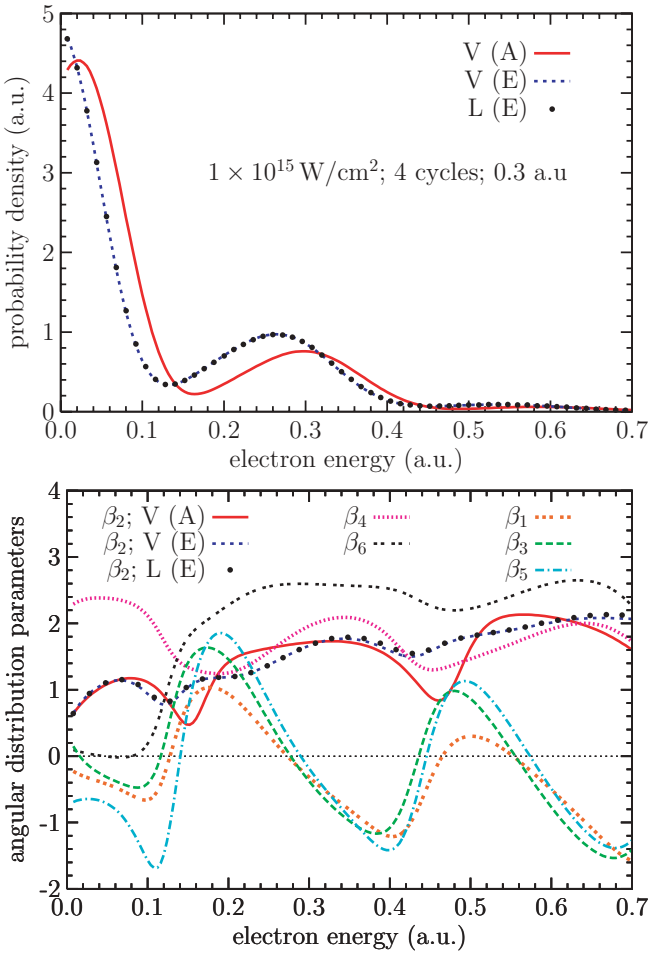

FIG. 2. (Color online) Photoelectron spectrum (top) and several asymmetry parameters (bottom) for ionization of atomic hydrogen in a four-cycle laser pulse with a $\sin^2$ envelope, a peak intensity of 1×10^{15} W/cm^2, and a central frequency of 0.3 a.u., corresponding to a wavelength of 152 nm. The calculations were performed with angular momenta up to $\ell_{\max} = 20$ in the length (L) and velocity (V) form of the electric dipole operator. Either the electric field ($\boldsymbol{E}$) or the vector potential ($\boldsymbol{A}$) were set to the $\sin^2$ envelope for the spectrum and the parameter β_2. For all other parameters, the $\sin^2$ envelope was used for the vector potential (see text for details).

of 1×10^{14} W/cm^2, and a central frequency of 0.114 a.u. (wavelength of 390 nm) are shown in Fig. 3.

Figure 4 shows the corresponding results for the spectrum and the angular distribution parameters β_1 and β_2. This is a more demanding problem, but it is still possible to obtain converged results for the ejected-electron spectrum with the length form of the electric dipole operator in the low-energy regime shown in these graphs, provided partial-wave contributions up to $\ell_{\max} \approx 60$ are taken into account.

The convergence in the angular distribution parameters (we only show β_2 and β_1 in the figures) is much less satisfactory in the length form. Not surprisingly, the biggest problems occur at energies that only very few of the ejected electrons have. Hence, this may not be too critical in practice, but it certainly sends a warning sign.

Regarding the physical interpretation of the results, we note that β_1 is very small in the vicinity of the maxima in

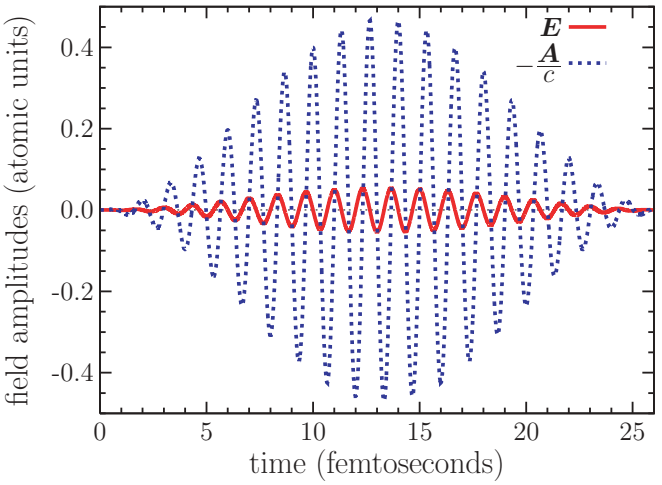

FIG. 3. (Color online) Electric field $\boldsymbol{E}(t)$ and vector potential $-\boldsymbol{A}(t)/c$ for a 20-cycle laser pulse with a $\sin^2$ envelope for $\boldsymbol{E}(t)$, a peak intensity of 1×10^{14} W/cm^2, and a central frequency of 0.114 a.u., corresponding to a wavelength of 390 nm.

the ejected-electron spectrum. This suggests that the angular distribution is more or less independent of the carrier envelope phase, which is not surprising given the rather long pulse. Both β_2 and β_1 exhibit rapid variations near the minima in the energy distribution, with the results obtained in the velocity form of the dipole operator being very stable with respect to increasing the number of partial waves. Hence we believe that these results are well converged.

We now move on to a serious challenge, namely, ionization by a strong infrared laser pulse. Figure 5 shows our results for three peak intensities, 4×10^{14} W/cm^2, 6×10^{14} W/cm^2, and 1×10^{15} W/cm^2 (bottom), for a 10-cycle laser pulse with a central frequency of 0.057 a.u., corresponding to a wavelength of 780 nm. Results for the lower two intensities were also presented by Madronero and Piraux [4]. In order to compare directly with their results, we used a $\sin^2$ envelope for the vector potential rather than the electric field.

Qualitatively we obtain very good agreement with their predictions, especially in the low-energy regime. We note, however, that the results shown in the insets of their Fig. 5 exhibit some rapid oscillations that seem to be of numerical rather than physical nature. With our radial mesh extending up to 3600 atomic units, we are essentially free of reflections, and those that might become a problem are easily eliminated by our gobbler starting at 3200 atomic units. However, the norm of our wave functions differs from unity by only about one part in a million at the end of the time propagation, thus indicating that the gobbler regime is hardly reached.

We note an excellent convergence with the number of partial waves. This issue was addressed by Madronero and Piraux as well, but they were not sure whether the differences between two sets of results presented in their Fig. 6 were due to the number of partial waves, the number of basis functions, or both. Looking at our results, we obtain very good agreement with those of Madronero and Piraux, already with "only" 50 partial waves in the expansion of the wave function. This finding on the convergence also holds for the highest intensity

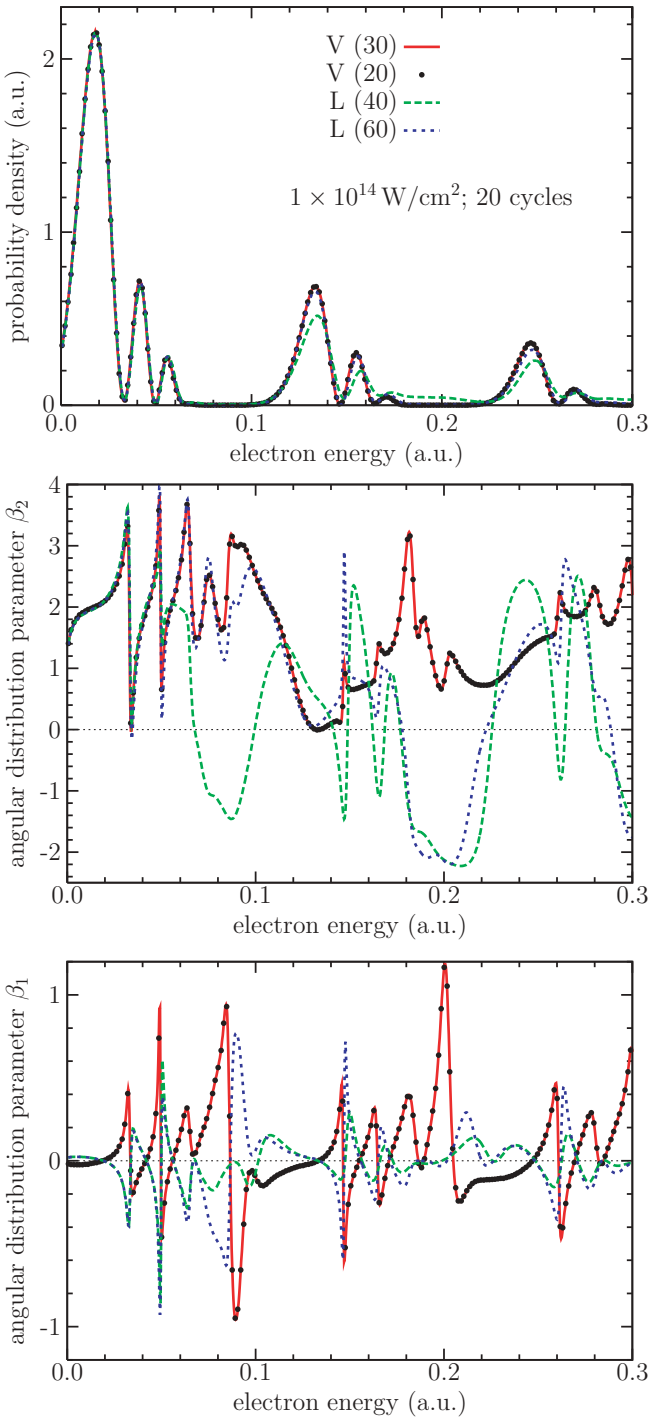

FIG. 4. (Color online) Photoelectron spectrum (top) and asymmetry parameters β_2 (center) and β_1 (bottom) for ionization of atomic hydrogen in a 20-cycle laser pulse with a $\sin^2$ envelope for the electric field, a peak intensity of 1×10^{14} W/cm^2, and a central frequency of 0.114 a.u., corresponding to a wavelength of 390 nm. The calculations were performed with the length (L) and velocity (V) forms of the electric dipole operator for angular momenta up to the values $\ell_{\max}$ indicated in the parentheses.

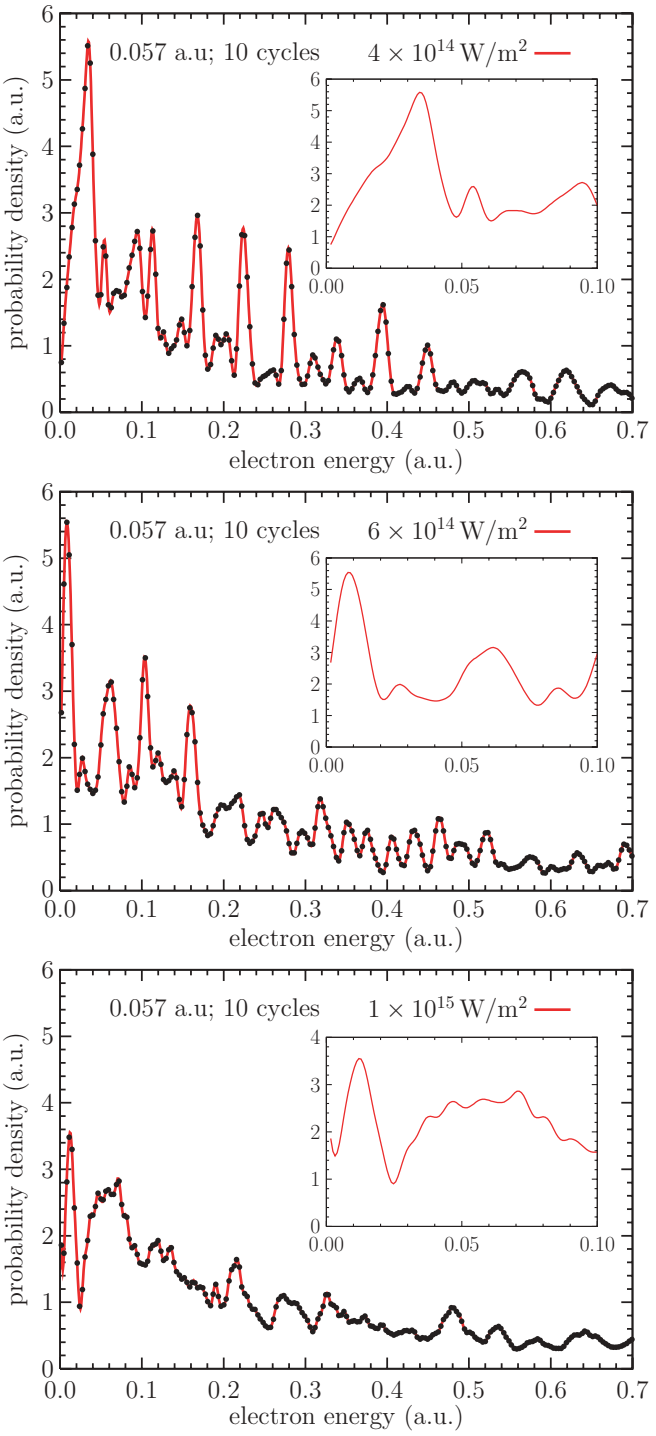

FIG. 5. (Color online) Photoelectron spectrum for ionization of atomic hydrogen in a 10-cycle laser pulse with a $\sin^2$ envelope for the vector potential, peak intensities of 4×10^{14} W/cm^2 (top), 6×10^{14} W/cm^2 (center), and 1×10^{15} W/cm^2 (bottom), and a central frequency of 0.057 a.u., corresponding to a wavelength of 780 nm. The calculations were performed with the velocity form of the electric dipole operator for angular momenta up to $\ell_{\max} = 70$ (solid line) and $\ell_{\max} = 50$ (dots). The inserts show the low-energy regime on an extended scale.

of 1×10^{15} W/cm^2 shown in the bottom panel of Fig. 5. This might seem surprising given the large ponderomotive energy of nearly 60 eV, which suggests that 40 photons would need to be absorbed for an electron to be emitted at all. The reason that one can still get converged results is simply the low probability of nearly always increasing the electron's angular momentum. Instead, the quantum mechanical selection rule of $\Delta\ell = \pm 1$

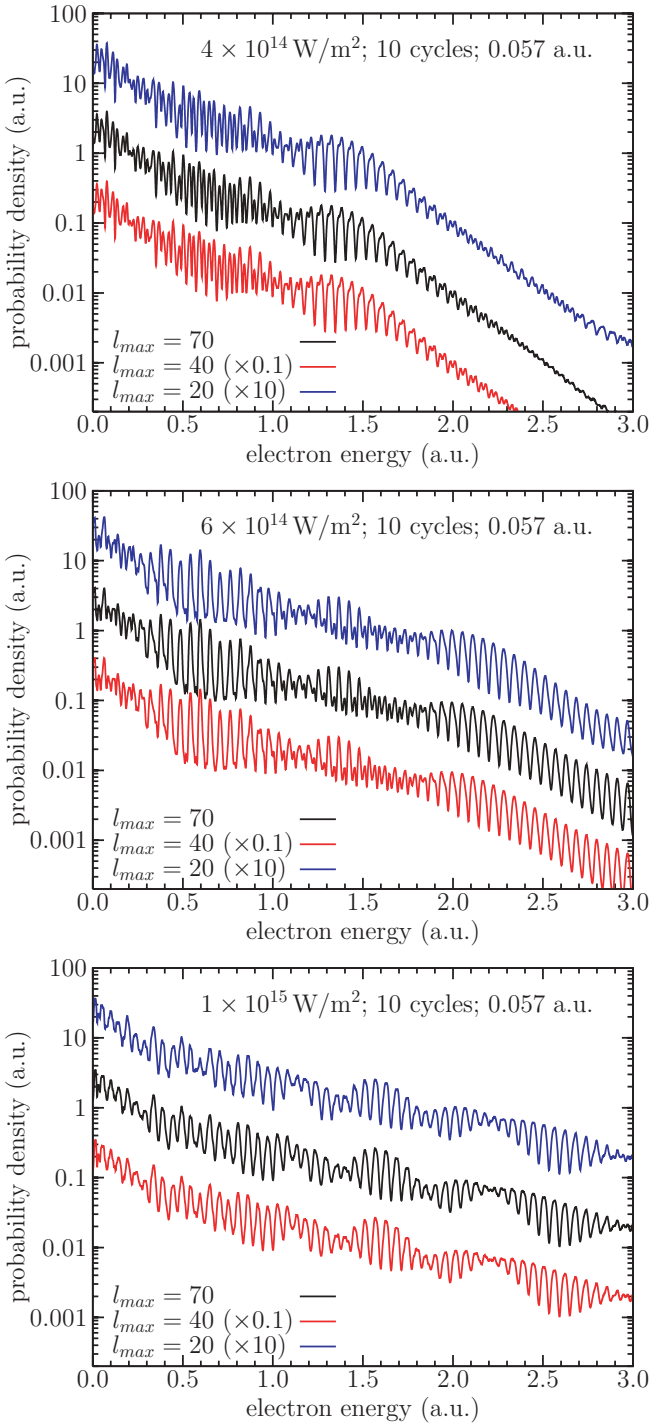

FIG. 6. (Color online) Photoelectron spectrum for ionization of atomic hydrogen in a 10-cycle laser pulse with a $\sin^2$ envelope for the electric field, peak intensities of 4×10^{14} W/cm^2 (top), 6×10^{14} W/cm^2 (center), and 1×10^{15} W/cm^2 (bottom), and a central frequency of 0.057 a.u., corresponding to a wavelength of 780 nm. The calculations were performed with the velocity form of the electric dipole operator for angular momenta up to $\ell_{\max} = 70, 40$, and 20. The results for $\ell_{\max} = 40(20)$ were multiplied by 0.1(10) to make them distinguishable from the $\ell_{\max} = 70$ results.

allows for a decrease as well, and hence it is possible to neglect the very high angular momenta and still obtain converged results as long as the velocity form of the dipole operator is being used. (See also the illustrations given by Cormier and Lambropoulos [10].) In other words, the lack of convergence in the length form is *not* simply due to the number of photons that need to be absorbed. Note that there are many irregular structures in the ejected-electron spectrum, but we believe that the results presented here are entirely physical.

Finally, we employed our code to investigate the spectrum up to even higher energies. Using a finite-difference rather than a finite-element method to represent the Hamiltonian, this is straightforward in the present approach, since we do not have to increase and then check the convergence with the number of basis functions. Figure 6 shows our results for electron energies up to 3 a.u. (about 80 eV). Here we chose the $\sin^2$ envelope for the electric field rather than the vector potential. Although the details are not shown, we note that once again it matters whether this simple envelope function is used for $\boldsymbol{A}(t)$ or $\boldsymbol{E}(t)$, and hence it will likely be very important to know the details of the pulse to a high degree of accuracy if a meaningful comparison between experiment and theory is ever going to be made for these situations.

Regarding the partial-wave convergence of the results, note that we can already get a very clear picture of the physics with only $\ell_{\max} = 20$, that is, far less than the number of photons required to push the electron out. It is interesting that the complicated structure in the emission spectrum becomes more regular with increasing electron energy, which is clearly visible for the lower peak intensities of 4×10^{14} W/cm^2 (top) and 6×10^{14} W/cm^2, respectively. For the highest peak intensity of 1×10^{15} W/cm^2, the spectrum over the entire energy range presented here remains complex, with the amplitude of the oscillations changing significantly with the ejected-electron energy. While we believe that these results are physical, cross-checks by other theoretical methods and certainly by experiment seem highly desirable.

We finish this article by plotting the angular distributions for electrons of a fixed energy, as calculated from the β parameters defined in Eq. (34). Figures 7 and 8 exhibit our results for selected energy ranges near some peaks in Figs. 2 and 4. Not surprisingly, most of the emission occurs along the polarization axis (note the different scales on the axes). For the longer and weaker pulse of Fig. 3, the angular distribution depicted in Fig. 7 is very symmetric, at least near the maximum of the emission. This indicates that the carrier phase envelope is not very important and, consequently, one would not expect a significant forward-backward asymmetry in the electron emission.

For the shorter and more intense pulse of Fig. 1, on the other hand, the angular distribution of Fig. 8 shows a clear forward-backward asymmetry. With a stabilized carrier envelope phase, one should be able to measure this asymmetry, even if electrons with a range of energies are detected. It is also worth noting that the two sides of the peak show an opposite asymmetry. Consequently, it may be advisable to experimentally stay on one side of a given peak in order to maximize the asymmetry signal.

Finally, Fig. 9 illustrates the electron density at a few times during the pulse. One can clearly see how the electron probability distribution is affected by the laser and how the very concentrated initial distribution spreads out. Note the cylindrical symmetry around the long-dashed axis due to the linear polarization of the laser light. We produced a movie

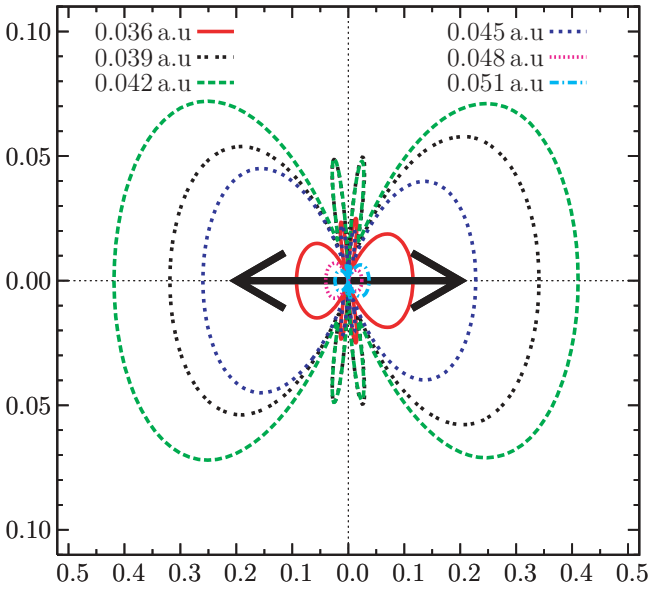

FIG. 7. (Color online) Angular distribution of electrons ejected with various energies (marked in the legend) by a 20-cycle laser pulse with a $\sin^2$ envelope for $\boldsymbol{E}(t)$, a peak intensity of 1×10^{14} W/cm^2, and a central frequency of 0.114 a.u., corresponding to a wavelength of 390 nm. The double arrow marks the linear polarization direction of the laser. Note the stretched scale on the axis perpendicular to the laser polarization. The distance from the origin is proportional to the size of the signal.

of this particular case that will be made available to interested readers upon request.

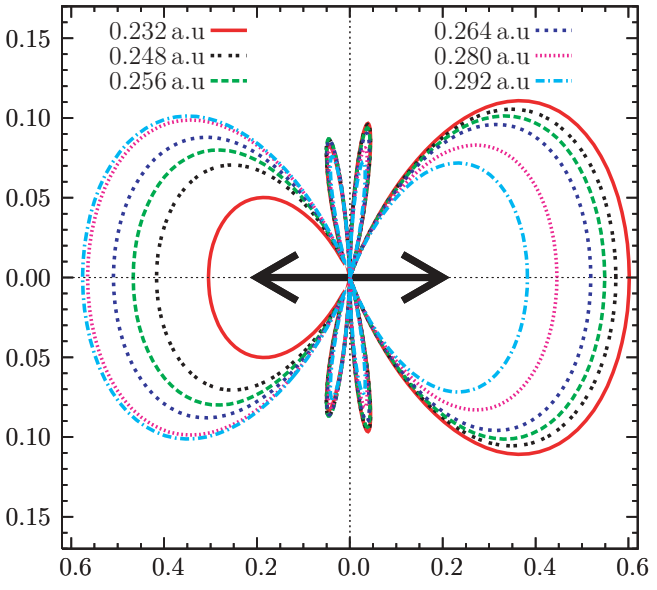

FIG. 8. (Color online) Angular distribution of electrons ejected with various energies (marked in the legend) by a four-cycle laser pulse with a $\sin^2$ envelope for $\boldsymbol{E}(t)$, a peak intensity of 1×10^{15} W/cm^2, and a central frequency of 0.3 a.u., corresponding to a wavelength of 152 nm. The double arrow marks the linear polarization direction of the laser. Note the stretched scale on the axis perpendicular to the laser polarization. The distance from the origin is proportional to the size of the signal.

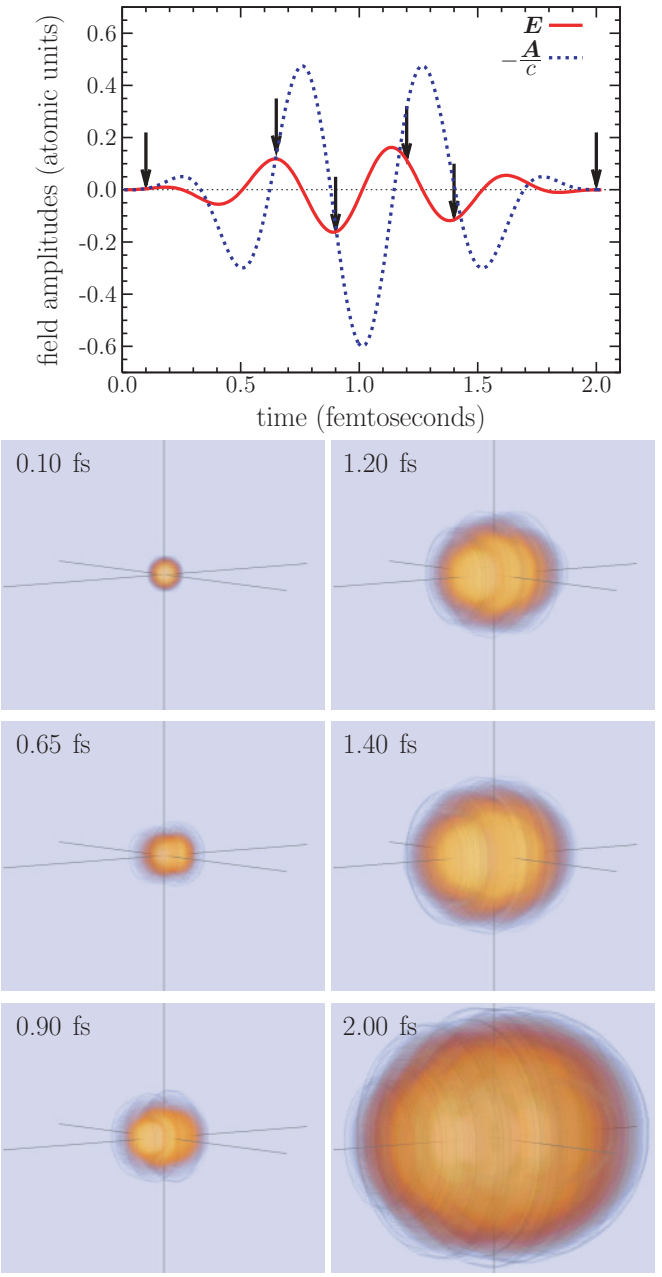

FIG. 9. (Color online) Electric field $\boldsymbol{E}(t)$ and vector potential $-\boldsymbol{A}(t)/c$ for a four-cycle laser pulse with a $\sin^2$ envelope for $\boldsymbol{E}(t)$, a peak intensity of 1×10^{15} W/cm^2, and a central frequency of 0.3 a.u., corresponding to a wavelength of 152 nm. This is the same as Fig. 1, with additional arrows marking the times for which the electron density is shown in the panels.

IV. CONCLUSIONS

Our implementation of the matrix iteration method of Nurhuda and Faisal [16] allows for the calculation of numerically stable results for the interaction of a short-pulse laser with the hydrogen atom. Although the principle of attacking this problem is well known, it remains a challenge for the case of intense infrared radiation, due to the large number of photons that need to be absorbed for the electron to be ionized.

After confirming results from previous work, we extended the parameter space into previously unchartered territory, where experimental investigations are currently in progress [19]. Employing the velocity form of the electric dipole operator and a large radial mesh to contain the wave function, we were indeed able to obtain converged results.

In addition to angle-integrated observables such as the ejected-electron spectrum, we made predictions for the angular distribution of electrons with a fixed energy. Finally, we visualized the time dependence of the process by plotting and animating the electron probability density.

The successful implementation of the matrix iteration method for the hydrogen atom interacting with strong infrared laser pulses opens the door to applications of the method to other physical problems, including those with more than one particle.

ACKNOWLEDGMENTS

This work was supported by the NSF under Grant PHY-0757755. A.N.G. gratefully acknowledges the hospitality of Drake University during his recent visit when this work was initiated.

[1] A. Rudenko, K. Zrost, C. D. Schröter, V. L. B. de Jesus, B. Feuerstein, R. Moshammer, and J. Ullrich, J. Phys. B **37**, L407 (2004).
[2] C. M. Maharajan, A. S. Alnaser, I. Litvinyuk, and C. L. Cocke, J. Phys. B **39**, 1955 (2006).
[3] Z. Chen, T. Morishita, A.-T. Le, M. Wickenhauser, X. M. Tong, and C. D. Lin, Phys. Rev. A **74**, 053405 (2006).
[4] J. Madronero and B. Piraux, Phys. Rev. A **80**, 033409 (2009).
[5] K. J. Schafer and K. C. Kulander, Phys. Rev. A **42**, 5794 (1990); **45**, 8026 (1992).
[6] K. LaGattuta, J. Opt. Soc. Am. B **7**, 639 (1990).
[7] K. J. LaGattuta, Phys. Rev. A **41**, 5110 (1990).
[8] L. Roso-Franco, A. Sanpera, M. L. Pons, and L. Plaja, Phys. Rev. A **44**, 4652 (1991).
[9] J. L. Krause, K. J. Schafer, and K. C. Kulander, Phys. Rev. A **45**, 4998 (1992).
[10] E. Cormier and P. Lambropoulos, J. Phys. B **29**, 1667 (1996).
[11] A. N. Grum-Grzhimailo, A. D. Kondorskiy, and K. Bartschat, J. Phys. B **39**, 4659 (2006).
[12] M. S. Pindzola and F. Robicheaux, Phys. Rev. A **57**, 318 (1998).
[13] A. K. Kazansky, J. Phys. B **31**, L579 (1998).
[14] J. Colgan, M. S. Pindzola, and F. Robicheaux, Phys. Rev. Lett. **93**, 053201 (2004).
[15] J. Fernández and L. B. Madsen, J. Phys. B **42**, 021001 (2009).
[16] M. Nurhuda and F. H. M. Faisal, Phys. Rev. A **60**, 3125 (1999).
[17] B. H. Bransden and C. J. Joachain, *Physics of Atoms and Molecules* (Pearson Education, Essex, UK, 2003), 2nd ed., Chap. 9.1.
[18] S. D. Conte and C. deBoor, *Elementary Numerical Analysis* (McGraw–Hill, New York, 1972).
[19] R. Sang and D. Kielpinski (private communication).